Journal of Alloys and Compounds 502 (2010) 231–237

Contents lists available at ScienceDirect

Journal of Alloys and Compounds

journal homepage: www.elsevier.com/locate/jallcom

Structural, dielectric properties and AC conductivity of $Ni_{(1-x)}Zn_xFe_2O_4$ spinel ferrites

Abdul Samee Fawzi, A.D. Sheikh, V.L. Mathe*

Novel Materials Research Laboratiry, Department of Physics, University of Pune, Ganeshkhind, Pune – 411007, Maharastra, India

ARTICLE INFO

Article history:
Received 28 December 2009
Received in revised form 21 April 2010
Accepted 23 April 2010
Available online 8 May 2010

Keywords:
Ni–Zn ferrite
XRD
SEM
Dielectric constant
Resistivity

ABSTRACT

The powders of Ni–Zn ferrite having the chemical formula $Ni_{(1-x)}Zn_xFe_2O_4$, where x varies as 0, 0.1, 0.2, 0.3, 0.4, and 0.5, were synthesized using solid state reaction method. The X-ray diffraction (XRD) studies confirmed the formation of spinel cubic structure. The average crystallite size was calculated using line broadening in XRD patterns. Also structural parameters like lattice constant (a), jump rate (L), polaron radius (r_p), bond lengths (R_A, R_B) and porosity (P) were determined from XRD data. The micro-structural features of the samples were studied using scanning electron microscopy (SEM) techniques. The variation of dielectric constant ($\hat{\varepsilon}$), loss tangent ($\tan\delta$) and AC conductivity (σ_{ac}) as a function of frequency in range of 100 Hz to 5 MHz was studied. Also the variation of dielectric constant and loss tangent as function of temperature was studied at fixed frequencies. The DC resistivity measurements of the samples were performed using two probe methods. The activation energies were computed from the plots of $\log \rho_{dc}$ versus $1000/T$.

1. Introduction

The nickel–zinc ferrite is a soft ferrite having low magnetic coercivity and high electrical resistivity. The high electrical resistivity and good magnetic properties make this ferrite an excellent core material for power transformer in electronic and telecommunication applications [1]. The Ni–Zn ferrites are commonly produced by conventional ceramic processes involving high temperature (≥1200 °C), solid state reactions between the constituent oxides/carbonates. The electronic structure of these materials may be qualitatively understood as a generalized Mott insulator [2]. In detail, the strong intra-site coulomb repulsion between '*d*' electrons splits the partially filled '*d*' band into upper and lower Hubbard bands, which results in an insulating electronic ground state and local magnetic moments at the same time [3]. Nickel ferrite ($NiFe_2O_4$) with an inverse spinel structure shows ferrimagnetism, which originates form magnetic moment of anti-parallel spins between Fe^{3+} ions at tetrahedral sites and Fe^{3+}, Ni^{2+} ions at octahedral sites [4]. In bulk Ni–Zn spinel ferrite Ni^{2+} occupies octahedral site whereas Zn^{2+} occupies tetrahedral site. Morrison et al. [5] have observed the presence of Zn^{2+} ions in octahedral sites in as prepared state itself when the material was prepared using micelle process having 7 nm size particles. The Neel temperature of $Ni_{0.5}Zn_{0.5}Fe_2O_4$ spinel ferrite was found to increase significantly from 538 K in the bulk state to 592 when the grain size was reduced to 16 nm [6]. The electrical properties of Ni–Zn ferrite have been studied by several investigators. Among them, Abdeen [7] has reported the AC and DC electrical conductivity in Ni–Zn ferrite. He was observed that DC and AC electrical conductivities increase as temperature increase transforming from ferrimagnetic to paramagnetic state on passing through Curie point. This indicates that the studied ferrite samples are magnetic semiconductors. The dependence of the anomalous electrical properties of nanocrystalline Ni–Zn ferrites upon composition and sintering temperature has been studied by Sheikh and Mathe [8]. Gul et al. [9] have observed the presence of Zn^{2+} ions causes appreciable change in the structural, magnetic and electrical properties. Shinde et al. [10] investigated the DC resistivity of Ni–Zn ferrites prepared by oxalate precipitation method. They obtained the high resistivity ferrites can be prepared by oxalate precipitation method with low sintering temperature and smaller duration as compared to ceramic and citrate precursor method. Mathe and Bhosale [11] investigated the effect of annealing on spray deposited Ni–Zn ferrite thin films. They obtained the synthesis of Ni–Zn spinel ferrite by spray pyrolysis method onto a glass substrate is feasible. The composition dependence of the conductivity of Ni–Zn ferrite is explained in terms of the cation valences and distribution by El-Sayed [12]. Temperature dependence of effective thermal conductivity and effective thermal diffusivity of Ni–Zn ferrites studied by Joshi et al. [13]. Costa et al. investigated the effect of the sintering temperature on the micro-structural evolution and magnetic properties of Ni–Zn ferrites prepared by combustion reaction [14].

* Corresponding author. Tel.: +91 020 2569 2678x320.
E-mail address: vlmathe@physics.unipune.ernet.in (V.L. Mathe).

0925-8388/$ – see front matter © 2010 Elsevier B.V. All rights reserved.
doi:10.1016/j.jallcom.2010.04.152

In the present work, $Ni_{(1-x)}Zn_xFe_2O_4$, where $x = 0.0$, 0.1, 0.2, 0.3, 0.4 and 0.5, named as A_1, A_2, A_3, A_4, A_5 and A_6, respectively, have been prepared by the solid state reaction method. The single phase of the prepared samples, its lattice parameter, average particle size, X-ray density, porosity and polaron radius have been determined using X-ray diffraction data. The surface morphological and average grain size was studied by scanning electron microscopy techniques. The average grain size (grain diameter) of the samples was determined from SEM micrographs by linear-intercept technique. Temperature and frequency dependence of dielectric constant ($\acute{\varepsilon}$) and dielectric loss ($\tan\delta$) for all compositions have been studied.

2. Experimental details

The Ni–Zn ferrites were prepared using the solid state reaction method. The powders of NiO, ZnO and Fe_2O_3 in the required stoichiometric proportion were thoroughly mixed and milled for 3–4 h. The second stage is pre-sintering, which involves heating of intimate mixture of raw materials in order to start reaction between initial ingredients. The pre-sintering helps in homogenization, to remove the absorbed gases and moisture, causes partial reaction of the oxides and tends to reduce the shrinkage during the final sintering. The powders were pre-sintered at 900 °C for 24 h. The pre-sintered powders were then milled to fine powder so as to reduce the particle size and to promote mixing of any unreacted oxides. These powders were then mixed with 1% polyvinyl alcohol as a binder and pressed into pellets having diameter of 10 mm and thickness of 2–3 mm using hydraulic press. The samples in the form of pellet were sintered at 1200 °C for 12 h. The sintering involves large-scale diffusion and erasing of gradients of chemical potentials, resulting in formation of product.

The single phase formation of the materials was confirmed by powder X-ray diffraction technique. X-ray diffractogram of all samples was recorded using an X-ray diffractometer (model Bruker D8 Advance). The SEM micrographs were recorded using scanning electron microscope (model JEOL JSM 6360). The capacitance (C_p) and loss tangent ($\tan\delta$) were measured by two probe method in the frequency range 100 Hz to 5 MHz at room temperature using precision LCR meter (Model HIOKI 3532-50 LCR Hi tester). The variation of dielectric constant and loss tangent with temperature were studied at four fixed frequencies viz, 1 kHz, 10 kHz, and 100 kHz and 1 MHz by recording the same parameters. The frequency dependent AC conductivity was calculated from dielectric constant and loss tangent data. The DC resistivity measurements of the samples were performed by means of a two probe method.

3. Results and discussion

3.1. Structural properties

The X-ray diffraction pattern of ferrite samples having general formula $Ni_{(1-x)}Zn_{(x)}Fe_2O_4$ where $x = 0$, 0.1, 0.2, 0.3, 0.4 and 0.5 are shown in Fig. 1. All the patterns were indexed using JCPDS data for $NiFe_2O_4$, Ni–Zn ferrite card no. (10-325) (8-234), which depict cubic spinel structure of Ni–Zn ferrite samples. There are no extra peaks indicating purity of the samples synthesized. The positions all the Bragg lines were used to obtain the interplanar spacing and these values were used to index the peaks. The graph of lattice parameter verses the function $F(\theta)$ (Nelson–Riley formula) [15] is given in Fig. 2, where

$$F(\theta) = \frac{1}{2}\left[\left(\frac{\cos^2\theta}{\sin\theta}\right) + \left(\frac{\cos^2\theta}{\theta}\right)\right] \quad (1)$$

straight line plots are obtained for all samples, extrapolating the lines to $F(\theta) = 0$ at $\theta = 90^\circ$ gives corrected value of lattice constant. The concentration dependence of the lattice constant (a) with an accuracy of ±0.02 Å was determined form XRD data for $x = 0$–0.5 and given in Table 1. It is clear from Table 1 that the doping greatly affects the lattice constant (a) for all samples. Usually, in a solid solution of spinels within the miscibility range, a linear change in the lattice constant with the concentration of the components is observed [16]. The slow linear increase in the lattice constant due to the replacement of Ni^{2+} (0.78 Å) ions by slightly larger Zn^{2+} ions with an ionic radius of (0.83 Å) in the system $Ni_{(1-x)}Zn_xFe_2O_4$. The results are in agreement with the reports in the literature [15].

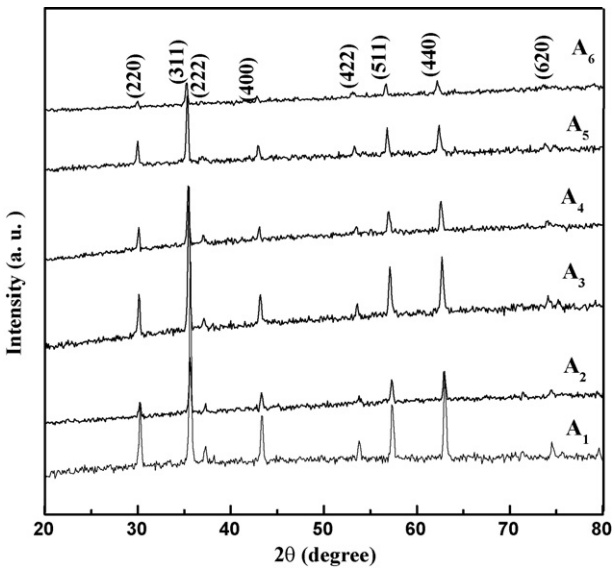

Fig. 1. X-ray diffraction patterns of A_1, A_2, A_3, A_4, A_5 and A_6.

The average crystallite size (D) obtained from the most intense line (3 1 1) was (18–27 nm) as estimated by Scherrer equation as follows [17].

$$D = \frac{K\lambda}{\beta\cos\theta} \quad (2)$$

where D is the average particle size, β is the full width of the diffraction line at half the maximum intensity, K is a constant (=0.9), λ is the wavelength, θ is the Bragg diffraction angle. The average crystallite size values and lattice strain (η) were determined from XRD line width using Scherrer formula modified by Williamson and Hall equation [18].

$$\frac{\beta\cos\theta}{\lambda} = \frac{1}{\varepsilon} + \frac{\eta\sin\theta}{\lambda} \quad (3)$$

where ε is the effective crystallite size, η is the strain introduced inside the sample and all other parameters are as defined in Eq. (2). Plot of $\beta\cos\theta/\lambda$ versus $\sin\theta/\lambda$ is shown in Fig. 3. The effective crystallite size and strain were calculated using a linear equation; $y = \eta x + 1/\varepsilon$, the slope of these lines gives strain while their intercept on y-axis shows the effective crystallite size. The effective crystallite size and the lattice strain obtained from the Williamson–Hall

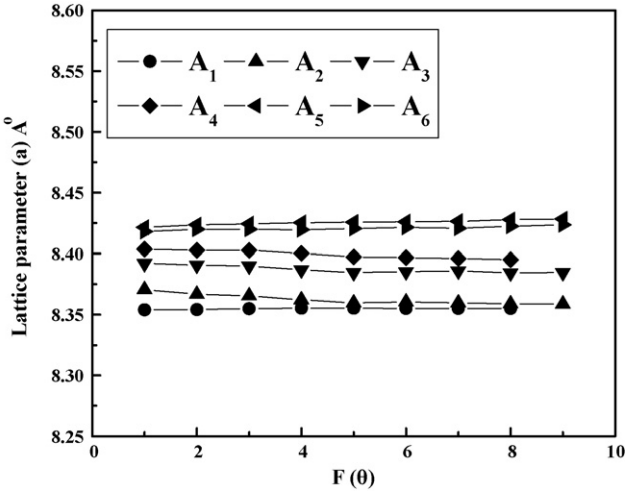

Fig. 2. The lattice constant versus the function $F(\theta)$.

Table 1
Lattice constant (a), effective crystallite size (ε), lattice strain (η), polaron radius (r_p), jump rate (L), X-ray density (ρ_x), actual density (ρ_a) and percentage porosity (p).

Samples	a (Å)	ε (nm)	η (%)	r_p (Å)	L (Å)	ρ_x (gm/cm^3)	ρ_a (gm/cm^3)	P (%)
A_1	8.34	11	3.8×10^{-3}	0.733	2.945	5.37	5.24	2.51
A_2	8.36	13.2	2.9×10^{-3}	0.735	2.955	5.34	5.13	3.89
A_3	8.38	15	2.6×10^{-3}	0.736	2.961	5.31	4.93	7.18
A_4	8.39	17.6	2.1×10^{-3}	0.738	2.966	5.29	4.84	8.61
A_5	8.40	18	2.3×10^{-3}	0.739	2.969	5.26	4.72	10.32
A_6	8.41	19	2.5×10^{-3}	0.740	2.973	5.23	4.51	13.78

plot are listed in Table 1. It is clear from the data in Table 1 that the doping does not greatly affect the effective crystallite size and the lattice strain inside the samples. Also variation in the crystallite size using Scherrer formula (2) and Williamson–Hall equation (3) are in close agreement with each other. Fig. 4 represents the relation between tetrahedral site radius (r_{tet}) and octahedral sites radius (r_{oct}) with the lattice parameter a. The radii of the tetrahedral (r_A) and octahedral (r_B) sites have been calculated by using the relation [19]

$$r_A = [C_{AZn}\, r(Zn^{2+}) + C_{AFe}\, r(Fe^{3+})] \quad (4a)$$

$$r_B = \tfrac{1}{2}[C_{ANi} r(Ni^{2+}) + C_{AFe} r(Fe^{3+})] \quad (4b)$$

where $r(Ni^{2+})$, $r(Zn^{2+})$, and $r(Fe^{3+})$, are the ionic radii of Ni^{2+}, Zn^{2+}, and Fe^{3+}, ions respectively, while C_{AZn}, and C_{AFe} in Eq. (4a) are the concentration of Zn^{2+} and Fe^{3+} ions on tetrahedral sites and C_{ANi} and C_{AFe} in Eq. (4b) are the concentration of Ni^{2+} and Fe^{3+} ions on octahedral sites. It is well known that there is a correlation between ionic radius and lattice parameter. It is seen from Fig. 4 that the lattice parameter increases with increasing tetrahedral site radius (r_A) and decreasing octahedral site radius (r_B). Observations from Fig. 5 indicate that with increasing Zn concentration, radius of tetrahedral site is increased whereas that of octahedral site is decreased, which in turn increases the lattice parameter. The results are in agreement with the reports in the literature [8]. The bond lengths (R_A, R_B) have been calculated using the relations $R_A = r_A + r(O^{2-})$, $R_B = r_B + r(O^{2-})$, where $r(O^{2-})$ is the radius of the oxygen ion (1.32 Å). The oxygen positional parameter or anion parameter (u) for each sample was calculated using the formula [19]

$$u^{3m} = \frac{1/4R^2 - 2/3 + [(11/48)R^2 - (1/18)]^{1/2}}{2R^2 - 2} \quad (5)$$

where $R = R_B/R_A$ are average bond lengths.

The data on radii of tetrahedral and octahedral sites, bond lengths and oxygen position parameter for all the samples are given in Table 2. It is seen from the data that the oxygen position parameter increases with increasing in Zn^{2+} concentration which causes increase in lattice parameter as observed from XRD data. The X-ray density ρ_x was calculated using the relation, $\rho_x = 8M/Na^3$, where M is the molecular weight of the ferrite sample, N is Avogadro's number and 'a' is lattice constant. Experimentally, the density was obtained using Archimedes principle. The weights of sample in air and xylene were recorded. The actual density (ρ_a) was calculated using the formula [8].

$$\rho_a = \frac{(W_{air} \times \rho_{liquid})}{(W_{air} - W_{liquid})} \quad (6)$$

where ρ_a is the actual density, W_{air} is the weight of pellet in air, W_{liquid} is the weight of pellet in liquid, and ρ_{liquid} is the density of liquid.

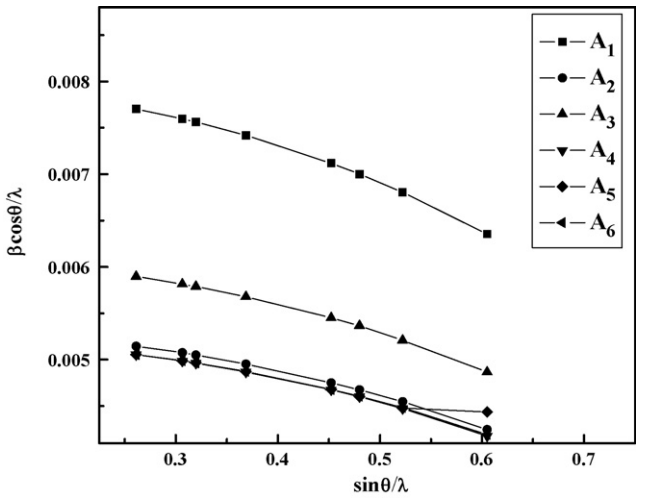

Fig. 3. Williamson–Hall plot of the A_1, A_2, A_3, A_4, A_5 and A_6.

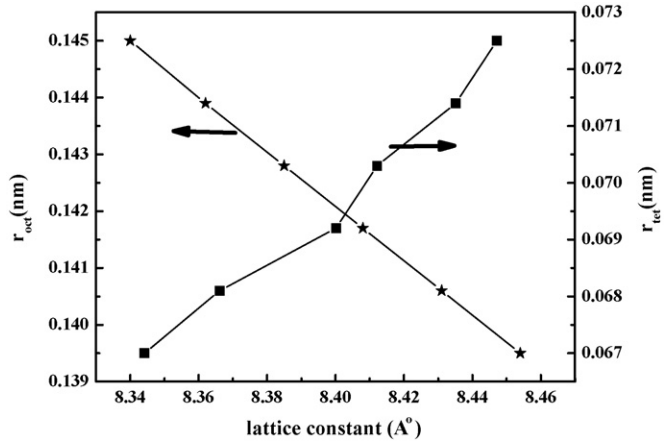

Fig. 4. Variation in tetrahedral site radius and octahedral site radius with lattice constant.

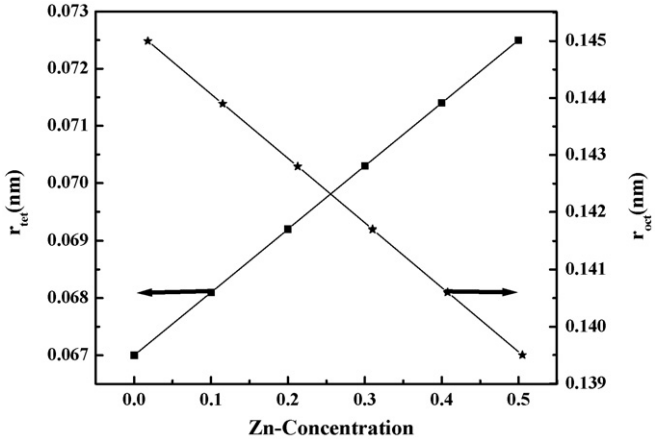

Fig. 5. Variation in tetrahedral site radius and octahedral site radius with Zn concentration.

Table 2
Cation distribution, bond lengths (R_A, R_B), ionic radius per molecule of the tetrahedral and octahedral sites (r_A, r_B) and oxygen position parameter (u).

Samples	Substance	Tetrahedral A sites	Octahedral B sites	R_A (Å)	R_B (Å)	r_A (Aɔ)	r_B (Aɔ)	u (Aɔ)
A_1	$NiO{\cdot}Fe_2O_3$	Fe^{3+}	$Ni^{2+}{\cdot}Fe^{3+}$	1.99	2.045	0.67	0.725	0.2600
A_2	$0.9NiO{\cdot}Fe_2O_3\,0.1ZnO{\cdot}Fe_2O_3$	$Zn^{2+}{}_{0.1}Fe^{3+}{}_{0.9}$	$Ni^{2+}{}_{0.9}{\cdot}Fe^{3+}{}_{1.1}$	2.006	2.0395	0.686	0.719	0.2610
A_3	$0.8NiO{\cdot}Fe_2O30.2ZnO{\cdot}Fe_2O_3$	$Zn^{2+}{}_{0.2}Fe^{3+}{}_{0.8}$	$Ni^{2+}{}_{0.8}{\cdot}Fe^{3+}{}_{1.2}$	2.022	2.034	0.702	0.714	0.2619
A_4	$0.7NiO{\cdot}Fe_2O_3\,0.3ZnO{\cdot}Fe_2O_3$	$Zn^{2+}{}_{0.3}Fe^{3+}{}_{0.7}$	$Ni^{2+}{}_{0.7}{\cdot}Fe^{3+}{}_{1.3}$	2.038	2.0285	0.718	0.708	0.2629
A_5	$0.6NiO{\cdot}Fe_2O_3\,0.4ZnO{\cdot}Fe_2O_3$	$Zn^{2+}{}_{0.4}Fe^{3+}{}_{0.6}$	$Ni^{2+}{}_{0.6}{\cdot}Fe^{3+}{}_{1.4}$	2.054	2.023	0.734	0.703	0.2638
A_6	$0.5NiO{\cdot}Fe_2O_3\,0.5ZnO{\cdot}Fe_2O_3$	$Zn^{2+}{}_{0.5}Fe^{3+}{}_{0.5}$	$Ni^{2+}{}_{0.5}{\cdot}Fe^{3+}{}_{1.5}$	2.07	2.0175	0.75	0.697	0.2648

The porosity of samples was determined by liquid immersion technique, using the formula:

$$\text{Percentage porosity} = \left(\frac{\rho_x - \rho_a}{\rho_x}\right) \times 100 \quad (7)$$

It is seen from Table 1 that the samples prepared are of good quality having experimental density values close to X-ray density.

In ferrites, the charge carriers are not completely free but are strongly localized in the *d*-shell; this localization may be due to formation of polarons. A small polaron defect is created when an electronic carrier gets trapped at given sites as a consequence of the displacement of adjacent atoms or ions. An attempt has been made to calculate the polaron radius for all the samples studied by the relation [20].

$$\gamma_P = \frac{1}{2}\left[\frac{\pi}{6N'}\right]^{1/3} \quad (8)$$

where N' number of sites per unit volume = $96/a^3$. Also we have calculated jump length (L) using relation [21].

$$L = a\frac{\sqrt{2}}{4} \quad (9)$$

The values of jump length for various values of Zn concentration are summarized in Table 1. This shows that jump length (L) and polaron radius (r_p) increases with increasing Zn concentration. The observed increase in L and r_p with Zn concentration suggests that charge carriers require more energy to jump from one cationic site to other.

The scanning electron micrographs of the two end members viz samples (A_1) and (A_6) are given in Fig. 6(a and b). The average grain size is estimated as ~1.57 μm for sample A_1 and that of sample A_6 are much bigger in size, which is estimated as 3.14 μm as seen in Fig. 6(a and b). This shows that particles grow substantially with the increase in Zn concentration. It is reported that zinc enhances the grain growth mechanism due to greater solubility in the solid state reaction at higher concentration. The compositional stoichiometry of the samples was curtained by EDAX.

3.2. Dielectric properties

The effect of frequency on dielectric constant ($\hat{\varepsilon}$) at room temperature for all samples is illustrated in Fig. 7(a). From Fig. 7(a), it is clear that dielectric constant decreased with increasing frequency and finally at higher frequencies attains almost constant value for all the samples. This is obvious because of the fact that the species contributing to the polarizability are lagging behind the applied field at higher frequency. The variation of dielectric constant with frequency reveals the dispersion due to Maxwell–Wagner [22,23] type interfacial polarization, which is agreement with Koop's phenomenological theory [24]. The large values of dielectric at lower frequency are mainly due to presence of all type of polarization i.e., $P_{total} = P_e + P_i + P_d + P_{sc}$ where subscripts indicate the electronic, ionic, dipolar and space charge contributions respectively. According to Sarah and Suryanarayana [25], the polarization in ferrites is through a mechanism similar to the conduction process. The exchange of electrons between ferrous ions (Fe^{2+}) and ferric ions (Fe^{3+}) on the octahedral site may lead to local displacement of electrons in the direction of applied field and these electrons determine the polarization. The polarization decreased with increasing frequency and then reaches a constant value due to the fact that beyond a certain frequency of external field the electron hopping cannot follow the alternating field.

Fig. 7(b) shows the dielectric loss ($\tan\delta$) as a function of frequency at room temperature for all samples. It can be seen that the dielectric loss decreases with increasing frequency [26]. The plot of ρ_{ac} with frequency is shown in Fig. 7(c). The AC resistivity is decreased with increasing in frequency at room temperature.

To understand the conduction mechanism and the hopping of charge carriers responsible for the conduction mechanism, the variation of ac conductivity as a function of frequency is calculated. Fig. 8 shows the variation $\log(\sigma_{ac} - \sigma_{dc})$ with $\log\omega^2$ for all samples. The nature of the graph is similar in all samples. It is well known that AC conductivity in disordered solids is directly proportional to frequency. The electrical conduction mechanism in terms of the electron and polaron hopping model has been discussed earlier by Austin and Mott [27] and Appel et al. [28]. Alder and Feinleib [29] have reported the frequency dependent electrical conductivity

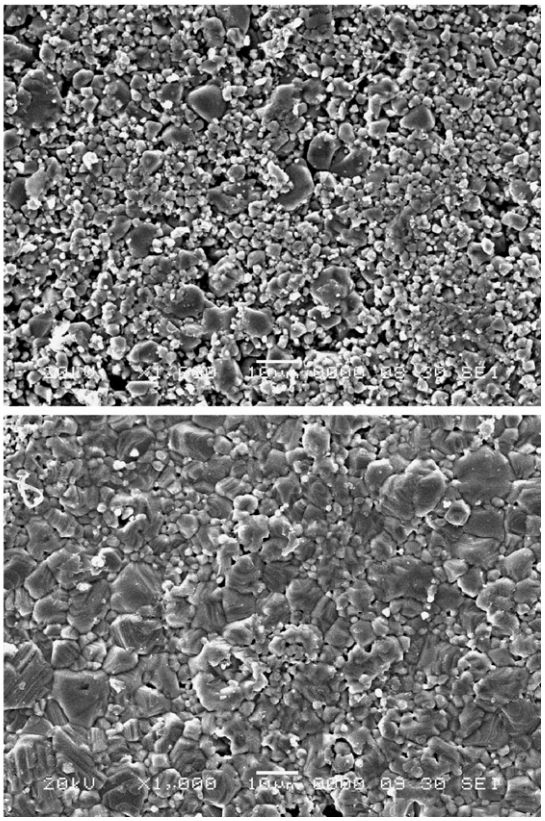

Fig. 6. (a and b) SEM micrograph of A_1 and A_6 samples.

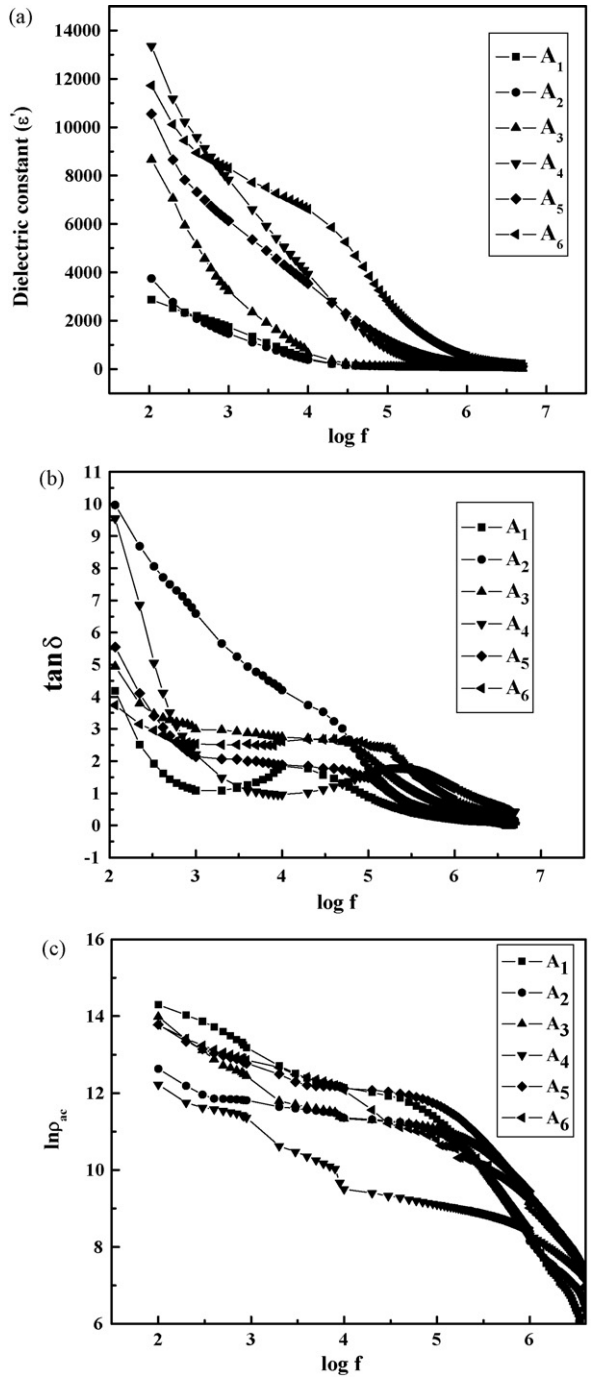

Fig. 7. Frequency dependent variation of (a) dielectric constant (b) loss tangent and (c) ac resistivity for Ni–Zn ferrite samples.

follows the relation

$$\sigma_{ac} - \sigma_{dc} = \frac{\omega^2 \tau}{1 + \omega^2 \tau^2} \quad (10)$$

where, ω is the angular frequency, τ is staying time (10^{-10} s) for all ceramics (if $\omega^2\tau^2 \ll 1$). The linearity of AC conductivity plot indicating that the conduction occurs by hopping of small polaron type of charge carriers among the localized states. At higher frequencies, where conductivity is increased greatly with frequency, the transport is dominated by contributions from hopping of infinite clusters [30].

Fig. 9(a) is showing the variation of dielectric constant ($\acute{\varepsilon}$) with temperature for A_2 sample. The dielectric constant gradually

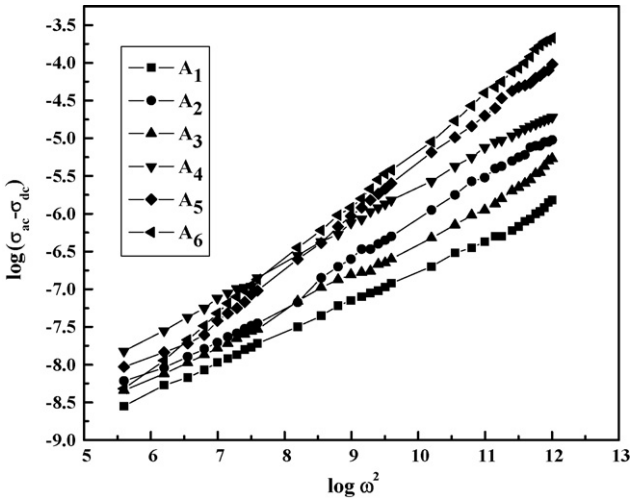

Fig. 8. Variation of AC conductivity with frequency for Ni–Zn ferrite samples.

increases with temperature at first and then decreases beyond a Curie temperature (T_C). The temperature dependent behavior of dielectric constant for ferrites can be explained as follows: dielectric constant in ferrites is attributed to four types of polarizations [25]: interfacial (P_i), dipolar (P_d), atomic (P_{sc}) and electronic (P_e). At low frequencies, all four types of polarizations contribute, the rapid increase in dielectric constant with temperature is mainly due to interfacial and dipolar polarizations, which are strongly temperature dependent [31]. In case of the interfacial polarization, this

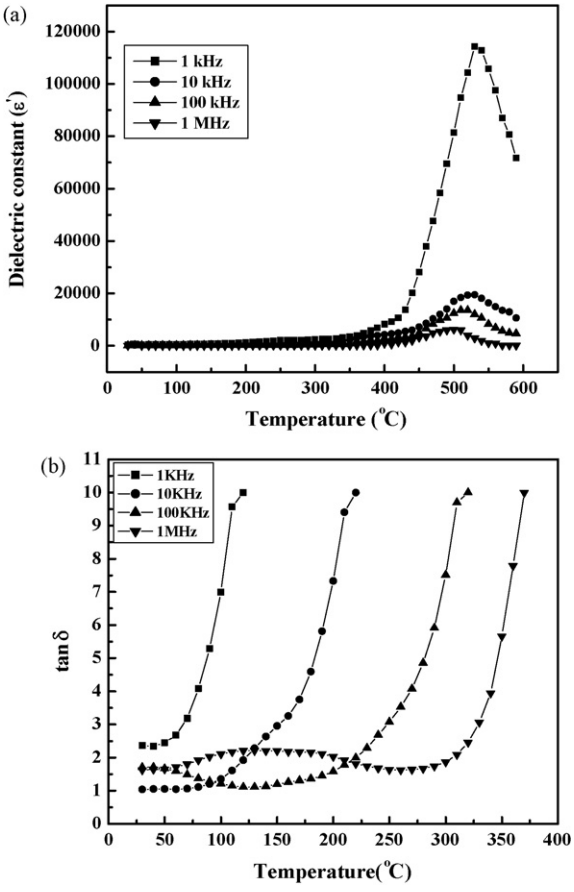

Fig. 9. Variation of (a) dielectric constant and (b) loss tangent with temperature for A_2 sample.

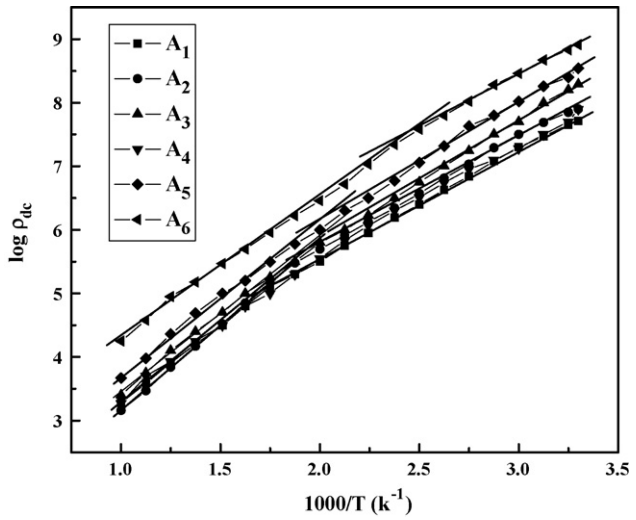

Fig. 10. Variation of DC resistivity with temperature for Ni–Zn ferrite samples.

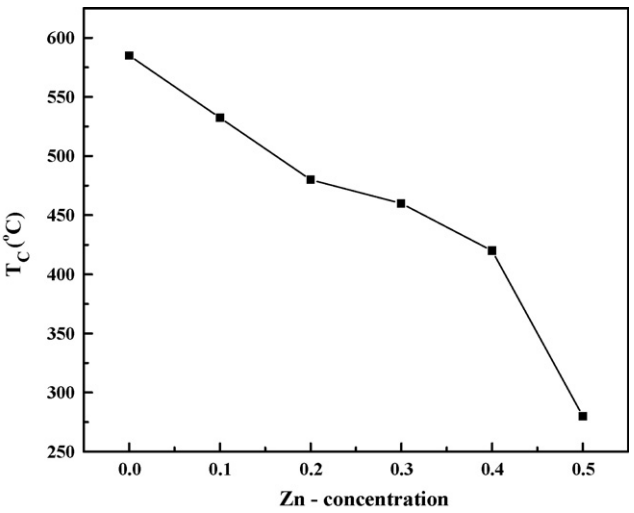

Fig. 11. Variation of Curie temperature (T_C) with Zn concentration.

is due to the accumulation of charges at the grain boundary, an increase in polarization results as more and more charges reach the grain boundary with increase in temperature.

Fig. 9(b) shows the variation of loss tangent ($\tan\delta$) with temperature for different frequencies for sample A_2 in which a pattern is similar to dielectric constant with temperature. As seen from Fig. 9(b), loss tangent is minimum at lower temperature and increased with increasing temperature. The increase in loss tangent is a result of the decreasing resistivity of the all samples with temperature. This curve can be understood on the basis of the Debye equation for loss tangent [32].

$$\tan\delta = \frac{\varepsilon'}{\varepsilon''} = \frac{1}{\omega\tau} \tag{11}$$

where ε'' = imaginary part of the permittivity, ω = the angular frequency, τ = the conductivity relaxation time

According to this equation, dielectric loss would be increase with decrease in relaxation time for a given frequency. Therefore, as the relaxation time decreases with increasing temperature and loss tangent also increases. However, with further increase in temperature, $\tan\delta$ shows a decline after a certain maximum value. An observed break in the plot is due to the instrumental limitation, as LCR bridge meter (model HIOKL 3532-50 LCR Hi TESTER) cannot record value of $\tan\delta$ greater than 10.

3.3. Electrical properties

The temperature dependent variation of DC resistivity for all samples is shown in Fig. 10. It is seen that the resistivity decreases linearly with increasing temperature within certain range of temperature measurements for all samples. The conduction mechanism in ferrites is explained on the basis of Verwey and de Bohr [33] mechanism that involves exchange of electrons between the ions of the same elements present in more than one valence state and distributed randomly over equivalent crystallographic lattice sites. The decrease in DC resistivity with increase in temperature is attributed to increase in drift mobility of the charge carriers. The value of DC resistivity found to increase with increasing Zn^{2+} concentrations in Ni–Zn ferrite. The observed increase in DC resistivity with increase Zn concentration may be attributed to decreased Fe^{2+} content due to incorporation of Zn in the lattice. The DC resistivity of the ferrites, in general, depends on the density, porosity, grain size and chemical composition of the samples [9,34]. Fig. 10 also shows two regions of conductivity (i.e., change in slope) with a single transition. It is clear that the transition from ferrimagnetic to paramagnetic state shifted towards lower temperature with the increase in Zn concentration, as shown in Fig. 10. The Curie temperature clearly correlates with the Zn concentration of the samples and decreases as the concentration of Zn increases. The decrease of T_C with an increasing Zn^{2+} concentration may be explained on the basis of modification of the A–B exchange interaction strength due to the change of the Fe^{3+} distribution between A and B sites. The decrease of the Curie temperature is due to the weakening of A–B interaction. This could be attributed to the increase in the distance between the moments of A and B sites which is confirmed by the increase in the lattice parameter with increasing Zn concentration [35]. The Curie temperature (T_C) versus Zn concentration for all the samples is given in Fig. 11.

3.4. Conclusions

Ni Zn ferrite samples synthesized using solid state reaction techniques have been investigated in depth from the point of view of structural, dielectric and electrical properties. In Ni–Zn ferrite lattice constant found to increase with increasing Zn concentration. Also the radius of octahedral sites, X-ray density, and experimental density found to decrease with increase Zn concentration but porosity and tetrahedral sites increase with increase Zn concentration. The average grain size varies from 1.57 to 3.14 μm, with variation of Zinc concentration in $Ni_{(1-x)}Zn_xFe_2O_4$ composites. The dielectric behavior is explained in terms of electron exchange between Fe^{2+} and Fe^{3+}, suggesting that the polarization due to heterogeneity of the samples. Dielectric constant variation with temperature shows peak behavior, which is associated with the magnetic transition temperature of Ni–Zn ferrite. The variation of DC resistivity with temperature shows two regions of conductivity for all samples. The change in slope of curves beyond transition temperature indicates the change in activation energy for all samples. The Curie temperature found to decrease with increase in Zn concentration.

Acknowledgments

ASF is thankful to ICCR, New Delhi and Ministry of Higher Education in Iraq for financial support. VLM is thankful to DST, New Delhi for the financial support.

References

[1] T. Abraham, J. Am. Ceramic. Soc. Bull. 73 (1994) 62.

[2] N.F. Mott, Proc. Phys. Soc. Lond. 49 (1937) 72.
[3] N.F. Mott, Phil. Mag. 6 (1961) 287.
[4] D.S. Erickson, J.O. Mason, J. Solid State Chem. 59 (1985) 42.
[5] S.A. Morrison, C.L. Cahill, E.E. Carpenter, S. Calvin, R. Swaminathan, M.E. McHenry, V.G. Harris, J. Appl. Phys. 95 (2004) 6392.
[6] N. Ponpandian, A. Narayansa Samy, C.N. Chinnas Samy, N. Sivakumar, M.J. Greenche, K. Chattopadhyay, K. Shinoda, B. Jeyadevan, K. Tohji, Appl. Phys. Lett. 86 (2005) 192510.
[7] A.M. Abdeen, J. Magn. Magn. Mater. 185 (1998) 199.
[8] A.D. Sheikh, V.L. Mathe, J. Mater. Sci. 43 (2008) 2018.
[9] I.H. Gul, W. Ahmed, A. Maqsood, J. Magn. Magn. Mater. 320 (2008) 270.
[10] T.J. Shinde, A.B. Gadkari, P.N. Vasambekar, Mater. Chem. Phys. 111 (2008) 87.
[11] V.L. Mathe, C.H. Bhosale, Indian J. Eng. Mater. Sci. 10 (2003) 166.
[12] A.M. El-Sayed, Mater. Chem. Phys. 82 (2003) 583.
[13] G.P. Joshi, N.S. Saxena, R. Mangal, Acta Mater. 51 (2003) 2569.
[14] A.C.F.M. Costa, E. Tortella, M.R. Morelli, R.H.G.A. Kiminamib, J. Magn. Magn. Mater. 256 (2003) 174.
[15] S.A. Mazen, A.E. Abd El-Rahim, B.A. Sabrah, J. Mater. Sci. 22 (1987) 4177.
[16] H.E. Zhang, B.F. Zhang., G.F. Wang, X.H. Dong, Y. Gao, J. Magn. Magn. Mater. 312 (2007) 126.
[17] Xian-Ming Liu, Shao-Yun Fu., J. Magn. Magn. Mater. 308 (2007) 61.
[18] K. Williamson, W.H. Hall, Acta Metall. 1 (1953) 22.
[19] N.H. Vasoya, V.K. Lakhani, P.U. Sharma, K.B. Modi, Ravi Kumar, H.H. Joshi, J. Phys.: Condens. Matter 18 (2006) 8063.
[20] A.J. Bosman, J.H. Van Dall., Adv. Phys. 1 (1970) 19.
[21] B. Gillot, F. Jemmali, Phys. Status Solidi (a) 76 (1983) 601.
[22] J.C. Maxwell, Electricity and Magnetism, Oxford University, Press, London, 1973.
[23] K.W. Wagner, Ann. Phys. 40 (1993) 818.
[24] C.G. Koops, Phys. Rev. 83 (1951) 121.
[25] P. Sarah, S.V. Suryanarayana, Indian J. Phys. 77 (2003) 449.
[26] Y.H. Tang, X.M. Chen, Y.J. Li, X.H. Zheng, Mater. Sci. Eng. B 116 (2005) 150.
[27] I.G. Austin, N.F. Mott, Adv. Phys. 18 (1969) 41.
[28] J. Appel, F. Seitz, D. Thurnbull, H. Ehrenreich, Solid State Phys. 21 (1968) 193.
[29] D. Adler, J. Feinleib, Phys. Rev. B2 3 (1970) 112.
[30] K.K. Patankar, V.L. Mathe, A.N. Patil, S.A. Patil, S.D. Lotke, Y.D. Kolekar, P.B. Joshi, J. Electroceram. 6 (2001) 115.
[31] Y. Zhi, A. Chen, J. Appl. Phys. 91 (2002) 794.
[32] L.L. Hench, J.K. West, Principles of Electronic Ceramics, John Wiley and Sons, New York, 1990, 202.
[33] E.J.W. Venvey, J. Chem. Phys. 24 (1947) 174.
[34] S.T. Mahmud, et al., J. Magn. Magn. Mater. 251 (2002) 292.
[35] V.R.K. Murthy, J. Sobhanadri, Phys. Status Solidi (a) 38 (1976) 647.